Signal Processing 180 (2021) 107867

Contents lists available at ScienceDirect

Signal Processing

journal homepage: www.elsevier.com/locate/sigpro

Open and closed anatomical surface description via hemispherical area-preserving map

Amita Giri[a,1], Gary P.T. Choi[b,1,*], Lalan Kumar[c]

[a] Department of Electrical Engineering, Indian Institute of Technology Delhi, New Delhi, India
[b] Department of Mathematics, Massachusetts Institute of Technology, Cambridge, MA, USA
[c] Department of Electrical Engineering and Bharti School of Telecommunication, Indian Institute of Technology Delhi, New Delhi, India

ARTICLE INFO

Article history:
Received 1 July 2020
Revised 30 September 2020
Accepted 28 October 2020
Available online 1 November 2020

Keywords:
Hemispherical harmonics
Area-preserving parameterization
Open body reconstruction
Closed body reconstruction

ABSTRACT

Spherical harmonics, one of the most widely used basis functions for shape description, rely heavily on a spherical parameterization of the given surface. Additionally, spherical harmonics based 3D modeling works well only for closed surfaces, while many anatomical structures are hemisphere-like open objects. Therefore, it is more natural to have a hemisphere-based approach for their shape description. In this work, we propose a novel framework for the shape description of open and closed hemisphere-like surfaces. We first develop two hemispherical area-preserving parameterization methods for simply-connected open and closed surfaces respectively, and then utilize the hemispherical harmonics basis functions to yield an accurate representation of hemisphere-like anatomical surfaces. We assess the performance of the proposed framework for the shape description of human head. In particular, 60 hemispherical anatomical surfaces (20 closed brain surfaces, 20 closed skull surfaces, and 20 open scalp surfaces) constructed from human head MRI scans are utilized for this purpose. For the three types of surfaces, our framework achieves a significant improvement in the surface reconstruction accuracy by 75%, 80% and 50% respectively when compared to the spherical harmonics based approach. This suggests that our new shape description framework can facilitate the biomedical analysis of hemisphere-like anatomical objects.

1. Introduction

An accurate representation of a three-dimensional (3D) geometry is crucial for structural analysis in many biomedical applications such as molecular recognition [1], detection of neurological disability [2,3], dipole localization accuracy improvement [4,5] and human body anatomical structure description [6]. Spherical harmonics (SH), a set of basis functions defined on the unit sphere $\mathbb{S}^2$, are widely used for shape modeling and analysis, including the development of rotation independent representations [7] and Shannon-type entropy-based reconstruction methods [8], the large-scale modeling of parametric surfaces [9], the modeling of complex morphological structures from continuous surface maps [10], the statistical analysis of brain structures [11,12], and the development of surface filters [13–16]. Because of their promising mathematical properties, SH have also been commonly applied in computer graphics for the modeling of bidirectional reflectance distribution functions (BRDFs) [17], image-based rendering and relighting [18], BRDF shading [19], distant lighting [20,21], lighting-invariant object recognition [22] and irradiance environment maps [23].

However, in medical shape analysis, there exists a wide range of hemisphere-like anatomical structures such as brain, skull and scalp, which are naturally parameterized using the upper hemisphere $\mathbb{S}^2_{z\geq 0}$ only [24]. The representation of such hemispherical objects using basis functions defined over the full spherical domain $\mathbb{S}^2$ introduces discontinuities at the boundary of the hemisphere and requires a large number of coefficients [25]. Also, the traditional SH methods work efficiently only for closed surfaces as open surfaces are not topologically equivalent to the sphere [26,27]. However, many hemisphere-like anatomical structures such as ventricles and atriums are open objects, for which the conventional closed shape descriptions introduce errors in their 3D reconstruction [28]. Therefore, it is more preferable to have a shape description framework that works for both open and closed hemispherical anatomical structures.

In [25], Gautron et al. developed the hemispherical harmonics (HSH) basis functions, which are derived from SH and defined

* Corresponding author.
E-mail address: ptchoi@mit.edu (G.P.T. Choi).
[1] A. Giri and G. P. T. Choi contributed equally to this work.

https://doi.org/10.1016/j.sigpro.2020.107867
0165-1684/

on the upper unit hemisphere $\mathbb{S}^2_{z\geq 0}$. In recent years, HSH have been applied to surface reconstruction [28], brain source localization [24], Helmholtz bidirectional reflectance basis [29] and detection of morphological changes [30].

A standard approach for 3D shape description via basis functions is to make use of surface parameterizations [31], which refer to the process of mapping a complicated surface in $\mathbb{R}^3$ onto a standardized parameter domain. It is well-known that in general any surface parameterization unavoidably induces distortions in either angle or area, or both [32,33]. A major class of surface parameterization methods are the conformal parameterizations, which aim at preserving the angles and hence the local geometry of the surfaces [34–37]. In particular, it is common to parameterize genus-0 closed surfaces onto the unit sphere [38–43], and simply-connected open surfaces onto the unit disk [44–48]. However, as mentioned in [31], it is more desirable to have a uniform parameterization for 3D surface reconstruction. While the above-mentioned conformal parameterization approaches are angle-preserving, they usually produce a large area distortion, making the parameterization results highly nonuniform and thereby hindering the surface reconstruction. In recent years, more efforts have been devoted to the development of area-preserving parameterization methods using Lie advection [49], optimal mass transport (OMT) [50–53], density-equalizing map (DEM) [54,55], and stretch energy minimization (SEM) [56]. However, the target parameter domains of these approaches are either the unit sphere or the unit disk. To utilize HSH for 3D shape description, it is necessary to have a method that parameterizes any given (open or closed) hemisphere-like surfaces onto the unit hemisphere.

In this work, we propose a novel framework for the surface description of both open and closed hemisphere-like anatomical surfaces via hemispherical area-preserving parameterizations and the HSH basis functions. We first develop two hemispherical area-preserving parameterization methods for simply-connected open and closed surfaces (which are topologically equivalent to the open hemisphere and the closed hemisphere) respectively, and then utilize the parameterization methods and the HSH basis functions to achieve an effective surface description. We apply the proposed framework for the reconstruction of closed brain surfaces, closed skull surfaces and open scalp surfaces, and compare our approach with the traditional SH approaches in terms of the reconstruction accuracy.

The rest of the paper is organized as follows. The anatomical dataset used in our work is introduced in Section 2. The background of the SH and HSH basis functions is provided in Section 3. In Section 4, we describe our proposed framework for open and closed anatomical surface reconstruction via hemispherical area-preserving parameterization. Experimental results are presented in Section 5. In Section 6, we discuss the significance of the results and possible future works. We conclude the paper in Section 7.

2. Dataset

60 hemispherical anatomical surfaces (20 closed brain surfaces, 20 closed skull surfaces, and 20 open scalp surfaces) are constructed using MRI scans from the Open Access Series of Imaging Studies (OASIS) human head MRI dataset [57] (see Fig. 1 for the procedure), with the MATLAB FieldTrip toolbox utilized [58]. The voxels of the MRI scans are first segmented into the three different tissues (brain, skull and scalp) using the `ft_volumesegment` function, which constructs a binary mask of each tissue type such that the voxels that belong to the tissue type are represented by 1 and all other voxels by 0 (see Fig. 1, second column). Then, we use the `ft_prepare_mesh` function to create surfaces based on the segmentation results of three tissue types (see Fig. 1, third column). The output surfaces are in the form of triangular meshes, each consisting of approximately 1500 vertices. All three types of open and closed surfaces are desired to be parameterized onto the unit hemisphere for achieving the HSH shape description.

3. Background

In this section, we introduce the traditional SH basis functions, followed by the HSH basis functions.

3.1. Spherical harmonics (SH)

Let $\Omega = [0, \pi] \times [-\pi, \pi]$ be the space of spherical coordinates for $\mathbb{S}^2$, where $[0, \pi]$ is the range for the elevation angle θ and $[-\pi, \pi]$ is the range for the azimuth angle ϕ. The real-valued SH functions $Y_n^m : \Omega \to \mathbb{R}$ of order n and degree m are defined as follows [59]:

$$Y_n^m(\theta,\phi) = \begin{cases} (-1)^{|m|}\sqrt{2}K_n^m \sin(|m|\phi)P_n^{|m|}(\cos\theta) & : m < 0, \\ (-1)^{|m|}\sqrt{2}K_n^m \cos(m\phi)P_n^m(\cos\theta) & : m > 0, \\ K_n^0 P_n^0(\cos\theta) & : m = 0, \end{cases} \quad (1)$$

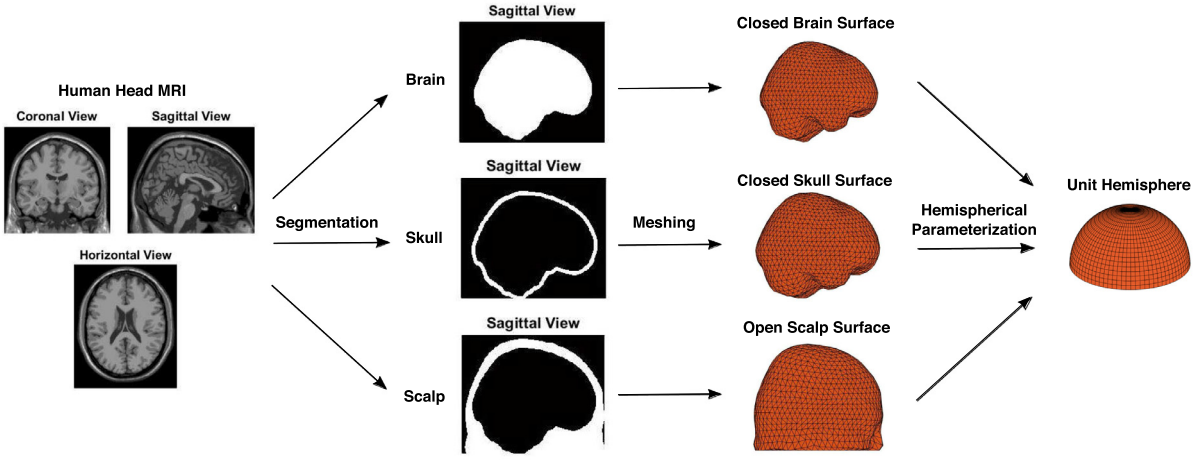

Fig. 1. A flow chart illustrating the process of constructing brain, skull and scalp surface from human head MRI scans. Subsequently, open (skull) and closed (brain and scalp) object surfaces are parameterized onto the unit hemisphere for the HSH shape description.

where K_n^m is a normalization constant given by

$$K_n^m = \sqrt{\frac{(2n+1)(n-|m|)!}{4\pi(n+|m|)!}}, \tag{2}$$

and P_n^m are the associated Legendre polynomials (ALPs):

$$P_n^m(x) = \frac{(-1)^m}{2^n n!}(1-x^2)^{m/2}\frac{\mathrm{d}^{n+m}}{\mathrm{d}x^{n+m}}(x^2-1)^n. \tag{3}$$

The ALPs for the same degree m and different orders n are orthogonal over the entire elevation range $\theta \in [0, \pi]$. The orthogonality relation is given as

$$\int_{-1}^{1} P_n^m(x) P_{n'}^m(x)dx = \frac{2(n+m)!}{(2n+1)(n-m)!}\delta_{nn'}, \tag{4}$$

where $x = \cos\theta \in [-1, 1]$, and δ is the Kronecker delta. Under the assumption of finite order, n takes value from 0 to N, where N is the prescribed maximum order, and the degree m varies from $-n$ to n. Thus, there are in total $(N+1)^2$ distinct orthonormal sets of basis functions.

3.2. Hemispherical harmonics (HSH)

The HSH basis functions are derived from SH for hemisphere-like objects, for which half of the sphere is unused. As an adapted version of the SH basis functions, the HSH basis functions are formulated by suitably shifting the ALPs such that they remain orthonormal but with a different normalization constant. The orthogonality relation in Eq. (4) is defined for a new range of elevation angles corresponding to the upper unit hemisphere $\mathbb{S}^2_{z\geq 0}$.

If the polynomials $P_n^m(x)$ are orthogonal over $[a, b]$, with $w(x)$ as a weighting function, then the polynomials $P_n^m(q_1x+q_2)$ with $q_1 \neq 0$ are orthogonal over an interval $\left[\frac{a-q_2}{q_1}, \frac{b-q_2}{q_1}\right]$, with $w(q_1x+q_2)$ as a weighting function and $q_1 \neq 0$ [60]. For a sector defined by $\theta \in [\theta_1, \theta_2]$, q_1 and q_2 can be obtained by solving the following system of equations:

$$\begin{cases} q_1\cos(\theta_2) + q_2 = a, \\ q_1\cos(\theta_1) + q_2 = b. \end{cases} \tag{5}$$

In particular, for $\mathbb{S}^2_{z\geq 0}$, the elevation angle takes value in $[0, \frac{\pi}{2}]$. Solutions to Eq. (5) for this new elevation range are utilized to express the shifted ALPs as $\widetilde{P}_n^m(x) = P_n^m(2x-1)$. The resultant shifted ALPs are now orthogonal over the interval $[0, 1]$, with the orthogonality relation given by

$$\int_0^1 \widetilde{P}_n^m(x)\widetilde{P}_{n'}^m(x)dx = \frac{(n+m)!}{(2n+1)(n-m)!}\delta_{nn'}. \tag{6}$$

Note that the ALPs are utilized for constructing the SH basis functions over the unit sphere. Analogously, the shifted ALPs are utilized herein for constructing the HSH basis functions over the upper unit hemisphere $\mathbb{S}^2_{z\geq 0}$. The real-valued HSH functions $H_n^m : [0, \pi/2] \times [-\pi, \pi] \to \mathbb{R}$ are defined as

$$H_n^m(\theta,\phi) = \begin{cases} (-1)^{|m|}\sqrt{2}\widetilde{K}_n^m \sin(|m|\phi)\widetilde{P}_n^{|m|}(\cos\theta) & : m < 0, \\ (-1)^{|m|}\sqrt{2}\widetilde{K}_n^m \cos(m\phi)\widetilde{P}_n^m(\cos\theta) & : m > 0, \\ \widetilde{K}_n^0\widetilde{P}_n^0(\cos\theta) & : m = 0, \end{cases} \tag{7}$$

where $\widetilde{K}_n^m$ is a normalization constant given by

$$\widetilde{K}_n^m = \sqrt{\frac{(2n+1)(n-|m|)!}{2\pi(n+|m|)!}}. \tag{8}$$

Similar to the SH basis functions, the HSH functions also form an orthonormal set of basis functions. The 3D plots of the HSH basis functions up to the second order ($N = 2$) are shown in Fig. 2. The distance between each surface point and origin indicates the magnitude of H_n^m, and the color represents the actual value of H_n^m. The HSH basis functions can be used for the surface reconstruction of objects that are effectively parameterized onto $\mathbb{S}^2_{z\geq 0}$. Given the hemispherical coordinates (θ, ϕ) of an object surface, we can reconstruct the surface using an appropriate number of HSH basis functions H_n^m, with $n \in [0, N]$ and $m \in [-n, n]$. For an error free representation of any object surface, the number of spatial sampling points k should be at least $(N+1)^2$ [61], which implies that $N \leq \sqrt{k} - 1$. In our work, N is chosen to be in the range of [1,25].

4. Proposed framework

In this section, we present a novel framework for efficient surface description via hemispherical area-preserving parameterization. To utilize the HSH basis functions, it is necessary to associate the hemispherical coordinates (θ, ϕ) with every point of the object surface. In other words, we need to establish a correspondence between the given surface and the upper unit hemisphere $\mathbb{S}^2_{z\geq 0}$. To achieve this, we propose two methods for computing the hemispherical area-preserving parameterizations for closed and open surfaces. The goal of the area-preserving parameterizations is to preserve the area of every triangular face as much as possible. Every object region is mapped to a region of proportional area in the parameter space, thereby yielding a homogeneous parameter distribution for the hemispherical shape description. The two proposed parameterization methods are outlined in Fig. 3. In both methods, the overall strategy is to flatten the input surface for reducing the 3D mapping problem to a 2D mapping problem, which is much easier to solve. The inverse stereographic projection is utilized as it provides a simple way for projecting a planar shape lying in the unit disk onto the upper unit hemisphere. Moreover, since the inverse stereographic projection has an explicit formula, we can easily take the area distortion induced by it into consideration when solving the 2D mapping problem. This ensures that we can obtain an area-preserving parameterization onto the hemisphere without dealing with a 3D mapping problem directly.

4.1. Hemispherical area-preserving parameterization for closed surfaces

Let $\mathcal{S}_c$ be a genus-0 closed surface discretized in the form of a triangulated mesh $(\mathcal{V}_c, \mathcal{F}_c)$, where $\mathcal{V}_c = \{v_1, v_2, \ldots, v_k\}$ is the vertex set and $\mathcal{F}_c$ is the face set (see Fig. 4(a)). We consider parameterizing $\mathcal{S}_c$ onto the closed unit hemisphere.

4.1.1. Choosing four base vertices

Note that a genus-0 closed surface is topologically equivalent to a closed hemisphere with the bottom plane included. Therefore, some points on the object surface will be mapped to the bottom plane of the hemisphere under a hemispherical parameterization in general. However, as the HSH basis functions are only defined on the curved part $\mathbb{S}^2_{z\geq 0}$, we need to ensure that no vertices will be mapped to the bottom plane. To achieve this, we start by choosing a pair of triangular faces $T_1 = [v_p, v_q, v_r], T_2 = [v_p, v_q, v_s] \in \mathcal{F}_c$ that share a common edge $[v_p, v_q]$ at the bottommost part of $\mathcal{S}_c$. Our goal is to map the four vertices $v_p, v_q, v_r, v_s \in \mathcal{V}_c$ onto the equator $z = 0$ of the unit hemisphere, and all other vertices onto the curved hemispherical surface. The bottom part of the hemisphere will then consist of the pair of triangular faces T_1, T_2 only. This specific setup ensures that none of the vertices lies at the bottom part of the closed unit hemisphere and hence the HSH basis functions are well-defined everywhere.

For the case of spherical parameterization, it was shown in [42] that choosing a triangular face as regular as possible is advantageous for getting a good parameterization onto a planar domain. For our case of hemispherical parameterization, we adopt

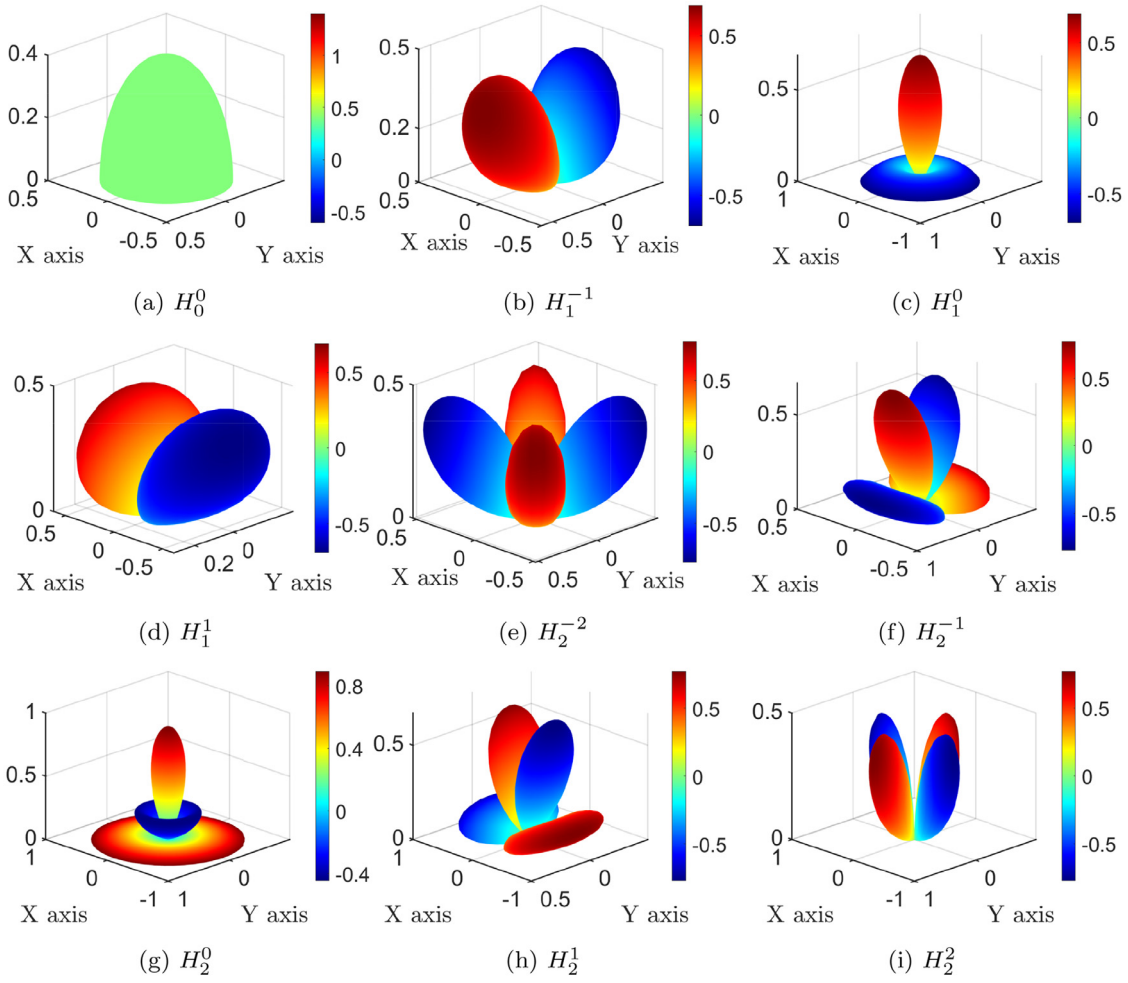

Fig. 2. The HSH basis functions up to the second order. (a) $n = 0$. (b)-(d) $n = 1$. (e)-(i) $n = 2$. The distance between each surface point and origin indicates the magnitude of H_n^m, and the color represents the actual value of H_n^m.

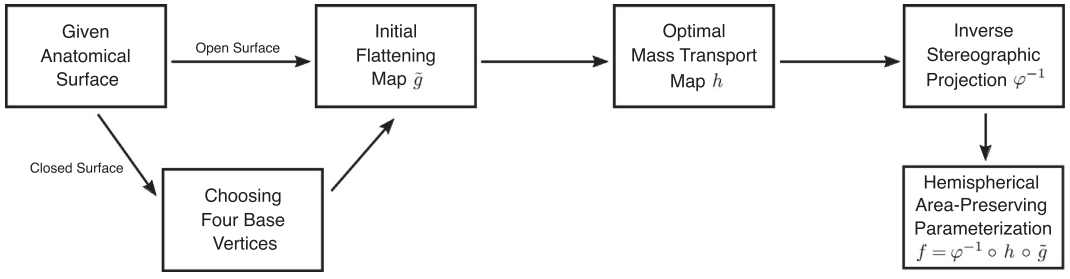

Fig. 3. The procedure of the proposed hemispherical area-preserving parameterization method for open and closed surfaces.

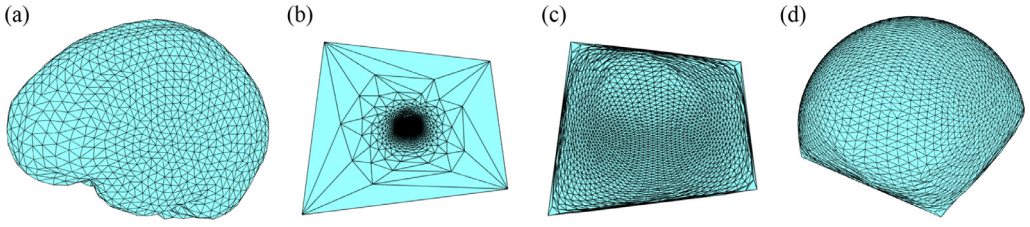

Fig. 4. An illustration of the hemispherical area-preserving parameterization for closed surfaces. (a) An input closed surface. (b) The initial flattening map obtained using the stretch energy minimization (SEM) method [56] combined with the quasi-conformal composition [42]. (c) The 2D optimal mass transport mapping result. (d) The final hemispherical parameterization result obtained using the inverse stereographic projection.

a similar strategy and choose the four vertices v_p, v_q, v_r, v_s at the bottommost part of $\mathcal{S}_c$ that yield a quadrilateral (formed by T_1, T_2) that is as close to a square as possible. More specifically, we first sort all edges according to the distance between their midpoints and the center of the bottom part of the surface (denote the sorted edges by $e_1, e_2, \ldots,$ with e_1 being the one closest to the center). Starting from $i = 1$, we consider the two triangles $[v_{p_i}, v_{q_i}, v_{r_i}], [v_{p_i}, v_{q_i}, v_{s_i}]$ with e_i being their common edge. We then evaluate the regularity of the quadrilateral formed by the four vertices $v_{p_i}, v_{q_i}, v_{r_i}, v_{s_i}$ by considering the ratio of the maximum side length to the minimum side length of the quadrilateral (denoted by r_{side}) and the ratio of the length of the longer diagonal to the length of the shorter diagonal of the quadrilateral (denoted by r_{diagonal}). If both r_{side} and r_{diagonal} are less than certain thresholds (which we set as 1.2 and 1.5 in practice), the four vertices are chosen as the base vertices. If not, we repeat the above process for the next e_i and so on. This automatic process ensures that the four vertices chosen are close to the center of the bottom part of the surface and yield a quadrilateral as regular as possible.

4.1.2. Initial flattening map

Consider $\mathcal{S}_c$ with the two chosen triangles T_1, T_2 punctured. The punctured surface is topologically equivalent to the plane and hence we can construct an initial flattening map of it onto a planar quadrilateral domain with the four corners corresponding to v_p, v_q, v_r, v_s. To reduce the area distortion of the flattening procedure, we first apply the stretch energy minimization (SEM) method [56], which looks for a map $g : \mathcal{S}_c \setminus \{T_1, T_2\} \to \mathbb{D} \subset \mathbb{C}$ that minimizes the stretch energy

$$E_{\text{SEM}} = \frac{1}{2}\mathbf{g}^* \mathbf{L}_g \mathbf{g}, \tag{9}$$

where $\mathbf{g} = [g(v_1), g(v_2), \ldots, g(v_d)]^t$, $\mathbf{g}^*$ is the conjugate transpose of $\mathbf{g}$, and $\mathbf{L}_g$ is the following modified Laplacian matrix:

$$(\mathbf{L}_g)_{ij} = \begin{cases} -w_{ij} & \text{if } [v_i, v_j] \text{ is an edge in } \mathcal{S}_c, \\ \sum_{l \neq i} w_{il} & \text{if } j = i, \\ 0 & \text{otherwise,} \end{cases} \tag{10}$$

with

$$w_{ij} = \frac{1}{4} \sum_{[v_i, v_j, v_k] \in \mathcal{F}_c} \frac{\overline{(g(v_i) - g(v_k))}(g(v_j) - g(v_k))}{\text{Area}([v_i, v_j, v_k])}. \tag{11}$$

In particular, the four vertices v_p, v_q, v_r, v_s are mapped onto the unit circle. To reduce the occurrence of highly skinny triangles in the mapping result, we compute the Beltrami coefficient μ of g, which is a complex-valued function that encodes the quasi-conformal distortion of the mapping [42]. The modulus of μ reflects the angular distortion of the mapping. In particular, a smaller $|\mu|$ indicates a smaller angle distortion. We then use the idea of quasi-conformal composition [42] and reconstruct a map with Beltrami coefficient $\lambda\mu$, where $\lambda \in [0, 1]$ is a balancing factor for controlling the conformality. This results in an initial flattening map $\tilde{g} : \mathcal{S}_c \setminus \{T_1, T_2\} \to \mathbb{R}^2$ with both area and angle distortion reduced (see Fig. 4(b)).

4.1.3. Optimal mass transport map

After obtaining the initial flattening map $\tilde{g}$, we compute a hemispherical area-preserving map using the optimal mass transport (OMT) mapping method. The OMT map requires setting the source and target area measures. As for the source measure, since the target domain is the unit hemisphere, it is necessary to take the conformal factor of the stereographic projection into consideration. Therefore, we set the source measure σ as follows [51]:

$$\sigma = \frac{4\ dx\ dy}{(1 + x^2 + y^2)^2}, \tag{12}$$

where (x, y) are the Cartesian coordinates of the plane. Since an area-preserving map is desired, we set the target measure τ at every vertex to be the normalized vertex area of $\mathcal{S}_c$ [51]:

$$\tau(v_i) = \frac{\sum_{i=1}^{k} 4A_{\tilde{g}(v_i)}/(1 + |\tilde{g}(v_i)|^2)}{\sum_{i=1}^{k} A_{v_i}} A_{v_i}, \tag{13}$$

where

$$A_{v_i} = \frac{1}{3} \sum_{T \in \mathcal{N}(v_i)} \text{Area}(T) \tag{14}$$

is the vertex area of v_i given by the area sum of all triangles T in the one-ring neighborhood $\mathcal{N}(v_i)$ of v_i divided by 3, and $A_{\tilde{g}(v_i)}$ is the vertex area of $\tilde{g}(v_i)$ defined analogously. Here, the normalization factor $\frac{\sum_{i=1}^{k} 4A_{\tilde{g}(v_i)}/(1+|\tilde{g}(v_i)|^2)}{\sum_{i=1}^{k} A_{v_i}}$ is used to appropriately rescale A_{v_i} so that the target measure is independent of the size of the input surface $\mathcal{S}_c$. This gives us an OMT map $h : \tilde{g}(\mathcal{S}_c \setminus \{T_1, T_2\}) \to \mathbb{R}^2$ with the source measure σ and target measure τ (see Fig. 4(c)).

4.1.4. Inverse stereographic projection

By applying the inverse stereographic projection

$$\varphi^{-1}(x, y) = \left(\frac{2x}{1 + x^2 + y^2}, \frac{2y}{1 + x^2 + y^2}, \frac{-1 + x^2 + y^2}{1 + x^2 + y^2} \right), \tag{15}$$

we obtain the composition map $f = \varphi^{-1} \circ h \circ \tilde{g}$. Since the OMT map h has taken the conformal factor of the stereographic projection into consideration, the mapping f is an area-preserving map of $\mathcal{S}_c \setminus \{T_1, T_2\}$ onto the unit hemisphere $\mathbb{S}^2_{z \geq 0}$. Finally, the two punctured triangles T_1, T_2 can be added back to the hemispherical parameterization result, thereby producing a closed hemispherical parameterization for $\mathcal{S}_c$ (see Fig. 4(d)). In particular, only the four vertices v_p, v_q, v_r, v_s lie on the equator $z = 0$, and all other vertices lie on $\mathbb{S}^2_{z>0}$.

4.2. Hemispherical area-preserving parameterization for open surfaces

Let $\mathcal{S}_o$ be a simply-connected open surface discretized in the form of a triangulated mesh $(\mathcal{V}_o, \mathcal{F}_o)$, where $\mathcal{V}_o$ is the vertex set and $\mathcal{F}_o$ is the face set (see Fig. 5(a)). In this case, our goal is to compute an area-preserving map of $\mathcal{S}_o$ onto the unit hemisphere $\mathbb{S}^2_{z \geq 0}$ with a hollow bottom part.

4.2.1. Initial flattening map

Since $\mathcal{S}_o$ is an open surface, we can directly compute an initial flattening map of it onto a planar domain without puncturing any triangles. Here, we apply the disk conformal parameterization method [46] to obtain a map $\tilde{g} : \mathcal{S}_o \to \mathbb{D}$ (see Fig. 5(b)). Note that the flattening procedure here is simpler than the one described above for the closed surface case. The reason is that for the closed surface case, the punctured surface only contains four boundary vertices, which unavoidably leads to a large distortion in the flattened domain and hence requires extra efforts to handle. By contrast, in the open surface case, the boundary vertices of $\mathcal{S}_o$ can be naturally mapped onto the boundary of the unit disk without producing a large distortion, and hence a simple procedure is sufficient for constructing a good initial flattening map. It may be noted that the initial flattening map in Fig. 5(b) is much less distorted when compared to the initial flattening map used in the closed surface case shown in Fig. 4(b) qualitatively. Employing the more complicated initial mapping procedure used in the closed surface case has little effect on the final parameterization result here.

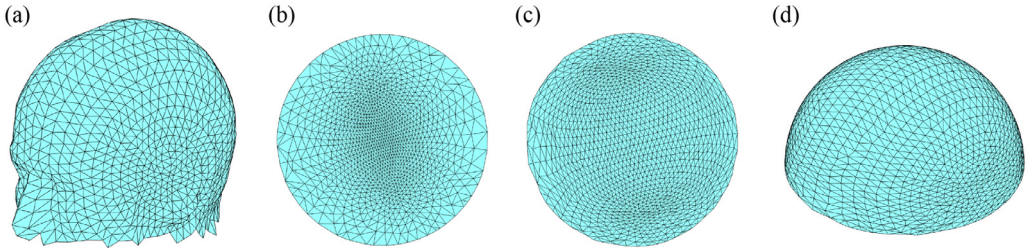

Fig. 5. An illustration of the hemispherical area-preserving parameterization for open surfaces. (a) An input open surface. (b) The initial flattening map obtained using the disk conformal parameterization method [46]. (c) The 2D optimal mass transport mapping result. (d) The final hemispherical parameterization result obtained using the inverse stereographic projection.

4.2.2. Optimal mass transport map

Once we have obtained the initial flattening map $\tilde{g}$, we simply follow the same approach as described in the closed surface case to construct an OMT map $h : \tilde{g}(\mathcal{S}_o) \to \mathbb{R}^2$ with the source measure σ given by Eq. (12) and the target measure τ given by Eq. (13) (see Fig. 5(c)).

4.2.3. Inverse stereographic projection

By applying the inverse stereographic projection φ^{-1} given by Eq. (15), we obtain the composition map $f = \varphi^{-1} \circ h \circ \tilde{g}$. Again, since the OMT map in the last step has taken the conformal factor of the stereographic projection into consideration, $f : \mathcal{S}_o \to \mathbb{S}^2_{z\geq 0}$ is an area-preserving map of the input open surface $\mathcal{S}_o$ onto the unit hemisphere $\mathbb{S}^2_{z\geq 0}$ (see Fig. 5(d)).

4.3. Hemispherical shape description

Let $\mathcal{S}$ be an open or closed hemisphere-like anatomical surface with k vertices, and $\mathbf{V} = (v_1, \dots, v_k)^T$ be a $k \times 3$ matrix of the vertex coordinates. Under the hemispherical area-preserving map f, each vertex $v = (x, y, z)$ on $\mathcal{S}$ is mapped to a point $f(v) = (x_f, y_f, z_f)$ onto the unit hemisphere $\mathbb{S}^2_{z\geq 0}$. The spherical coordinates (θ, ϕ) of $f(v)$ are given by

$$\theta = \cos^{-1} \frac{z_f}{\sqrt{x_f^2 + y_f^2 + z_f^2}} \quad \text{and} \quad \phi = \tan^{-1} \frac{y_f}{x_f}. \tag{16}$$

The parameterization defines the object surface through the mapping

$$v(\theta, \phi) = (x(\theta, \phi),\ y(\theta, \phi),\ z(\theta, \phi)). \tag{17}$$

The object surface can be expressed using the HSH basis functions as follows:

$$v(\theta, \phi) = \sum_{n=0}^{\infty} \sum_{m=-n}^{n} C_n^m H_n^m(\theta, \phi), \tag{18}$$

where $C_n^m = [(C_x)_n^m, (C_y)_n^m, (C_z)_n^m]$ is a 3-dimensional coefficient vector. Under the finite order assumption, n takes value from 0 to N and hence we have the following approximation:

$$v(\theta, \phi) \approx \sum_{n=0}^{N} \sum_{m=-n}^{n} C_n^m H_n^m(\theta, \phi). \tag{19}$$

Eq. (19) can be written as

$$\mathbf{V} = \mathbf{HC}, \tag{20}$$

where $\mathbf{C} = (C_0^0, C_1^{-1}, C_1^0, \cdots, C_N^N)^T$ is the HSH coefficient matrix, and $\mathbf{H}$ is a $k \times (N+1)^2$ matrix whose ith row is defined as

$$(\mathbf{H})_i = [H_0^0(\theta_i, \phi_i), H_1^{-1}(\theta_i, \phi_i), \cdots, H_N^N(\theta_i, \phi_i)]. \tag{21}$$

The HSH coefficients provide a measure of spatial frequencies constituting the object surface, with the higher frequency components containing more detailed attributes of the object surface. Theoretically, the coefficients are given by

$$C_n^m = \int_0^{\pi/2} \int_0^{2\pi} v(\theta, \phi) H_n^m(\theta, \phi) \sin\theta d\theta d\phi. \tag{22}$$

In practice, if only samples of the underlying continuous spatial function are available, we can estimate the coefficient matrix $\mathbf{C}$ in Eq. (20) by finding the unique least squares estimate using the Moore-Penrose pseudo-inverse:

$$\mathbf{C} = (\mathbf{H}^T\mathbf{H})^{-1}\mathbf{H}^T\mathbf{V}. \tag{23}$$

Using the estimated HSH coefficients and the HSH basis functions, we can effectively reconstruct the object surface.

5. Experimental results

The proposed hemispherical area-preserving parameterization and HSH reconstruction methods are implemented in MATLAB. We compute the hemispherical area-preserving parameterizations of the 20 brain, 20 skull and 20 scalp surfaces, initialized with the balancing factor $\lambda = 0.2$. Each mapping takes 2 seconds on average on a PC with an Intel i7-6700K CPU and 16 GB RAM.

5.1. Hemispherical parameterization and surface reconstruction

Figs. 6, 7 and 8 show three examples of closed brain, closed skull and open scalp surfaces (top left) and their hemispherical

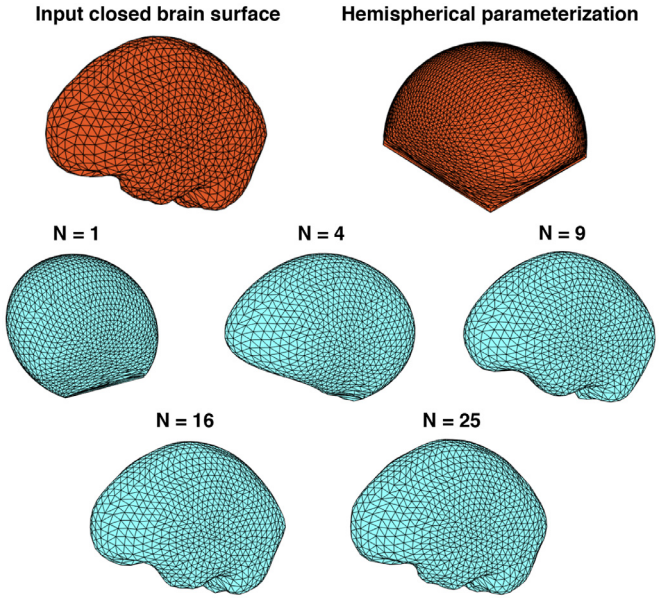

Fig. 6. A closed brain surface (top left), the hemispherical area-preserving parameterization (top right), and the HSH reconstructions with maximum order $N = 1, 4, 9, 16, 25$ (bottom).

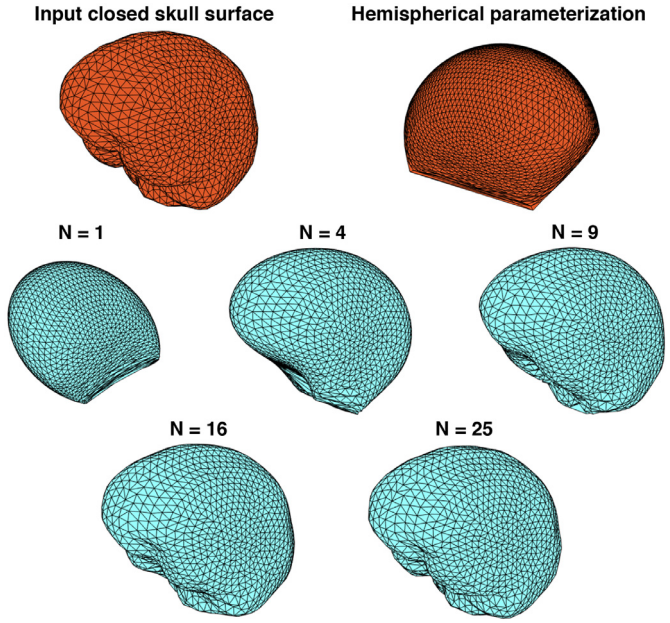

Fig. 7. A closed skull surface (top left), the hemispherical area-preserving parameterization (top right), and the HSH reconstructions with maximum order $N = 1, 4, 9, 16, 25$ (bottom).

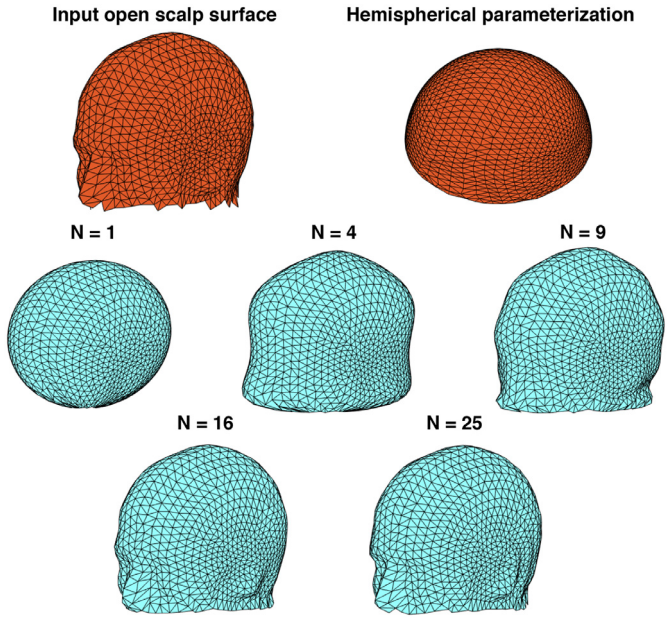

Fig. 8. An open scalp surface (top left), the hemispherical area-preserving parameterization (top right), and the HSH reconstructions with maximum order $N = 1, 4, 9, 16, 25$ (bottom).

area-preserving parameterizations (top right). As the parameterizations are area-preserving, it can be observed that the vertices are homogeneously distributed on the surfaces, thereby facilitating the hemispherical shape description. From the HSH reconstruction results with different maximum order $N = 1, 4, 9, 16, 25$ (bottom), it can be observed that our proposed framework effectively reconstructs all three types of hemisphere-like anatomical surfaces.

5.2. Reconstruction error

For a more quantitative analysis, we compare the surface reconstruction errors obtained using the hemispherical area-preserving parameterization together with the HSH basis functions and the traditional SH basis functions for different maximum order N. The reconstruction error e is defined as the Euclidean 2-norm of the difference between the original vertices and the reconstructed vertices:

$$e = \|\mathbf{V}_{\text{reconstructed}} - \mathbf{V}\|_2, \tag{24}$$

where $\mathbf{V}_{\text{reconstructed}}$ is the coordinate matrix of all vertices of the reconstructed surface. Fig. 9 shows the plots of e versus N for the brain, skull and scalp surfaces. It can be observed that for all three types of open and closed hemisphere-like surfaces, the reconstruction error can be effectively reduced using our HSH approach as N increases. On the contrary, the traditional SH basis functions lead to fluctuating reconstruction results and hence are less useful for handling these surfaces. In particular, we observe that the large surface reconstruction errors by SH correspond to globally distorted results instead of localized distortions (see Fig. 10 for an example). A possible explanation is that for the SH reconstruction, artificial oscillations start to appear when higher order basis functions are incorporated. At higher frequencies, the number of measurements may be insufficient, thereby leading to spatial aliasing errors [62]. When compared to HSH, the SH reconstruction error is much more significant at high frequencies, with higher order coefficients being aliased to lower order.

5.3. Statistical analysis

We further compare the reconstruction errors achieved by our HSH approach and the SH approach with the maximum order $N = 25$ in more details. For the 20 closed brain surfaces, 20 closed skull surfaces and 20 open scalp surfaces, the mean reconstruction error by our HSH approach is lower than that by the SH approach by 75%, 80% and 50% respectively as presented in Table 1. We apply the two-sample t-test on the two sets of error values for each type of surface and find that the improvements are statistically significant for all three types of surfaces. The relatively small improvement for the open surface case can possibly be explained by the fact that the boundary of the hemispherical parameterization is smoother when compared to that for the closed surface case, and hence the problem of discontinuities at the hemisphere boundary for SH [25] is less severe. Overall, the results suggest that our proposed HSH approach outperforms the traditional SH approach for the shape description of both open and closed hemisphere-like anatomical surfaces.

5.4. External validation using anatomical landmarks

For the open scalp surfaces, there are three prominent anatomical landmarks commonly used in electroencephalography (EEG), namely the nasion point, the left pre-auricular (LPA) point, and the right pre-auricular (RPA) point [63] (see Fig. 11(a)). As the proposed method is landmark-free, the three anatomical landmarks can be used for the external validation of our method. For each of the 20 scalp surfaces, we evaluate the mismatch error between the position of each landmark on the original surface and the estimated position of it obtained by the HSH or SH representation, with the maximum order $N = 25$. From the box plots of the landmark mismatch errors (Fig. 11(b)), it can be observed that the HSH approach achieves a smaller error for all three landmarks. This external validation experiment again demonstrates the advantage of our approach over the traditional SH approach.

5.5. Evaluation as a statistical shape model

To evaluate the proposed HSH approach as a statistical shape model, we consider performing a binary classification experiment

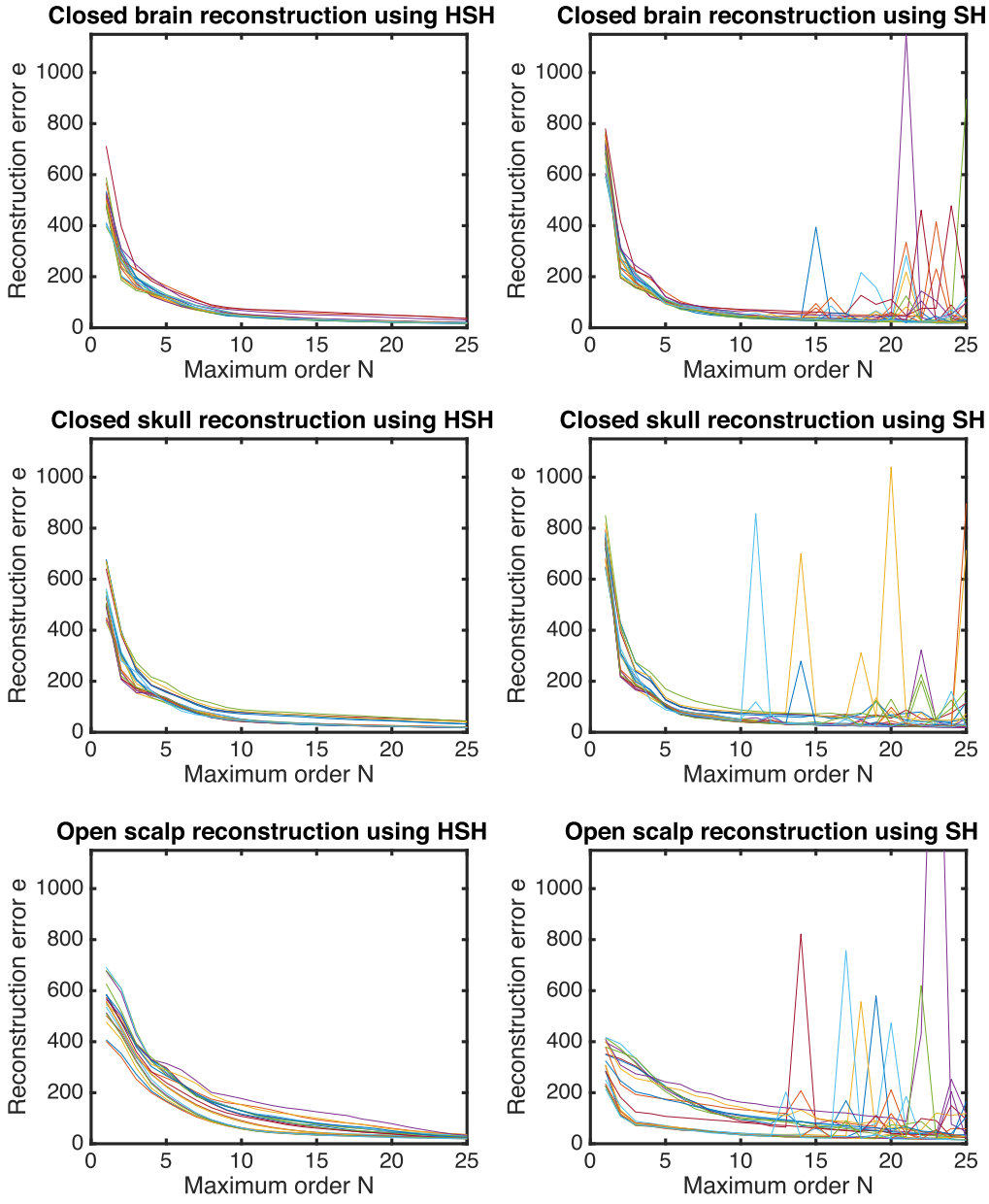

Fig. 9. The surface reconstruction error by the HSH basis functions and the SH basis functions with varying maximum order N. In each plot, each curve corresponds to one surface.

for distinguishing between the closed brain/skull surfaces and the open scalp surfaces using the HSH/SH representations. More specifically, given the maximum order N, we compute the $(N+1)^2 \times 3$ HSH/SH coefficient matrix for each of the 60 surfaces in the dataset. We then use the 2-norm of the difference between the coefficient matrices as a measure of the shape dissimilarity to classify the 60 surfaces. For each trial ($i = 1, 2, \ldots, 60$), we leave the i-th surface out and use the remaining 59 surfaces as training data for determining the label (open/closed) of the left-out surface. We then use the result of the 60 trials to determine the overall classification accuracy. Even for $N = 3$ (i.e. only the first $(3+1)^2 = 16$ basis functions are used), the HSH approach achieves a classification accuracy of 82%, while the traditional SH approach yields 53% only. For $N = 5$, the HSH approach achieves an accuracy of 91% while the SH approach yields 61% only. This shows that the proposed HSH approach is more effective in capturing the shape difference between the surfaces using a small number of coefficients.

5.6. Comparison with the SH approach via spherical parameterization

For the case of closed surfaces, one may also be interested in further comparing our proposed HSH reconstruction approach with a more conventional SH reconstruction method based on spherical parameterization. Here we use the spherical parameterization method [39] to parameterize the closed brain surface in Fig. 6 and then compute the reconstruction using the SH basis functions. From Fig. 12, it can be observed that the combination of spherical parameterization together with the SH basis functions does not lead to a good reconstruction result. In particular, the reconstruction of the bottom part of the brain surface is poor even if a large N is used, which can possibly be explained by the non-spherical geometry of the input brain surface. Comparing the results with the ones produced by our hemispherical approach shown in Fig. 6, it can be observed that our method produces more accurate reconstruction results. For a more quantitative comparison, we eval-

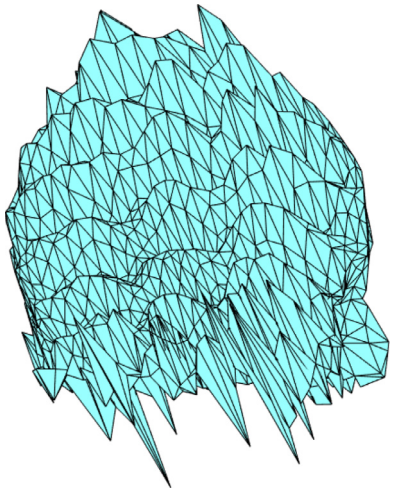

Fig. 10. The scalp surface reconstruction using SH of maximum order $N = 19$ shows global distortion.

Table 1
Statistical analysis of the average reconstruction error (mean e) achieved by the HSH approach and the SH approach with the maximum order $N = 25$.

Surface	Mean e		Improvement	Two-sample
	SH	HSH	by HSH	t-test
Brain	88.6	20.9	75%	$P < 0.01$
Skull	126.3	24.0	80%	$P < 0.01$
Scalp	51.4	25.8	50%	$P = 0.015$

uate the reconstruction error produced by the SH approach via the spherical parameterization for the 20 closed brain surfaces and the 20 closed skull surfaces (see the error plots in Fig. 13). The mean reconstruction error by our HSH approach is lower than that by the SH approach via the spherical parameterization by 70% and 65% for the brain and skull surfaces respectively. The two-sample t-test shows that the improvements are statistically significant (both with $P < 0.01$). This suggests that our proposed method is more suitable for hemisphere-like surface description.

5.7. Handling more complicated surfaces

One may wonder whether our proposed framework is applicable to more complicated surfaces. Here we consider a brain cortical surface reconstructed from MRI images in the OASIS dataset [57] using the open source reconstruction software FreeSurfer. As shown in Fig. 14, even for the highly convoluted cortical surface with deep sulci and gyri, our proposed method is capable of producing very accurate reconstruction results. We remark that for surfaces with a more complex shape, more iterations may be needed in the optimal mass transport step for correcting the area distortion produced by the initial flattening map.

6. Discussion

While genus-0 surfaces are topologically equivalent to the sphere, a spherical parameter domain may not be the most natural one for many anatomical surfaces with a hemispherical shape. The combination of the proposed hemispherical area-preserving parameterization methods and the HSH basis functions provides an effective way for handling hemisphere-like surfaces. Moreover, while most of the prior approaches have only focused on closed surfaces, our approach is capable of handling both open and closed surfaces.

Although we have only applied our proposed framework for brain, skull and scalp surfaces in our experiments, our method may also be advantageous for handling other anatomical structures such as hippocampus, bone and atrium. As these structures do not have a spherical shape, the proposed HSH approach may be more suitable than the traditional SH approach for the shape description and reconstruction of them. We plan to validate this hypothesis by applying our method on datasets of these structures in future works.

As we have demonstrated in our experiments, the HSH representations produce accurate reconstruction results for both open and closed hemisphere-like structures. Therefore, the proposed method can be effectively applied to the rendering, remeshing, and multiresolution modeling of hemisphere-like surfaces. Our method also provides a convenient way for analyzing the shape dissimilarities of hemisphere-like surfaces via their HSH representations.

Similar to other parameterization-based shape description approaches, our method relies on a pairwise mapping to a hemisphere primitive which treats each surface separately and does not incorporate information from the entire population. This limitation in ignoring the population-level statistics may lead to suboptimal models in certain statistical modeling and analysis tasks [64]. In our future work, we plan to explore methods for overcoming this limitation, possibly by incorporating certain population-level information in the computation of the hemispherical parameterization, and compare the result with the existing non-parameterization-based representations such as the deformation-based representation [65] and the particle system-based representation [66].

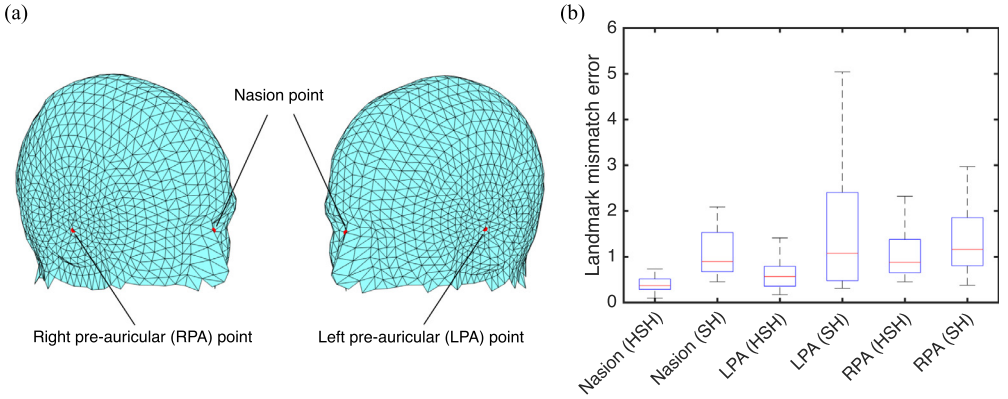

Fig. 11. (a) The three anatomical landmarks (the nasion point, the left pre-auricular point, and the right pre-auricular point) on each of the 20 open scalp surfaces. (b) The box plots of the landmark mismatch errors produced by the HSH approach and the SH approach with the maximum order $N = 25$ (right). For each approach and each of the three landmarks, the box plot shows the minimum, first quartile, median, third quartile, and the maximum of the 20 error values.

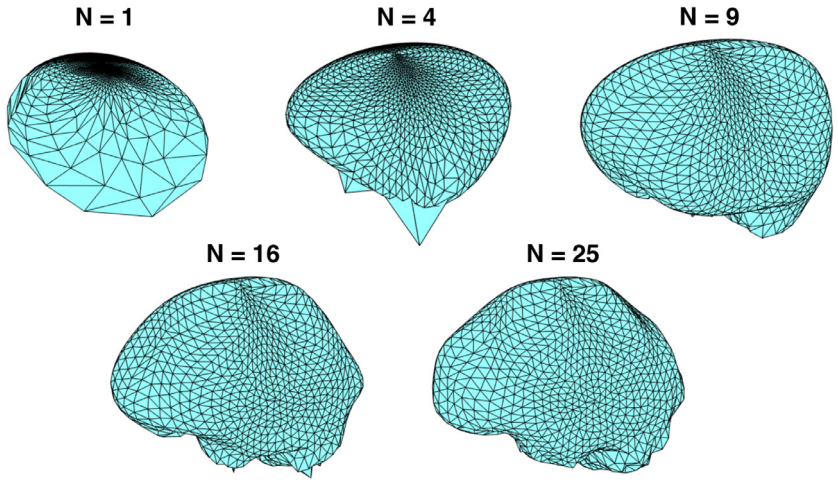

Fig. 12. The surface reconstruction of the closed brain surface in Fig. 6 achieved using the spherical parameterization [39] and the SH basis functions, with varying maximum order N.

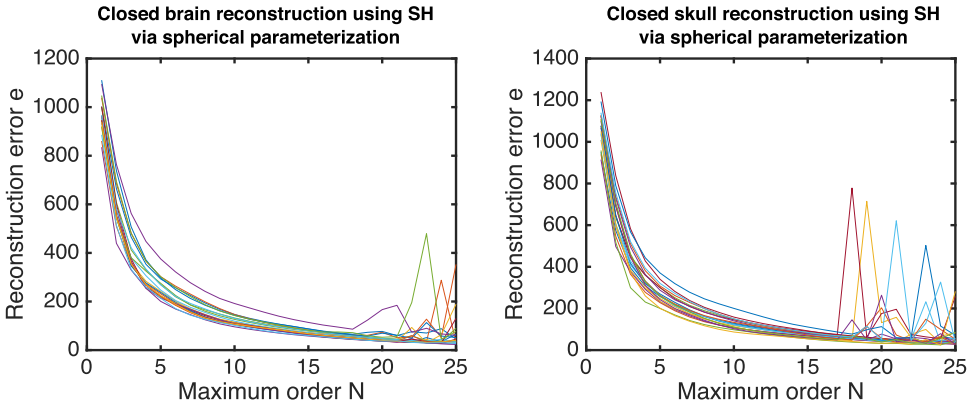

Fig. 13. The surface reconstruction error obtained by the SH approach via the spherical parameterization with varying maximum order N for the 20 closed brain surfaces and the 20 closed skull surfaces. In each plot, each curve corresponds to one surface. For comparison, see the error achieved by the proposed HSH approach in Fig. 9.

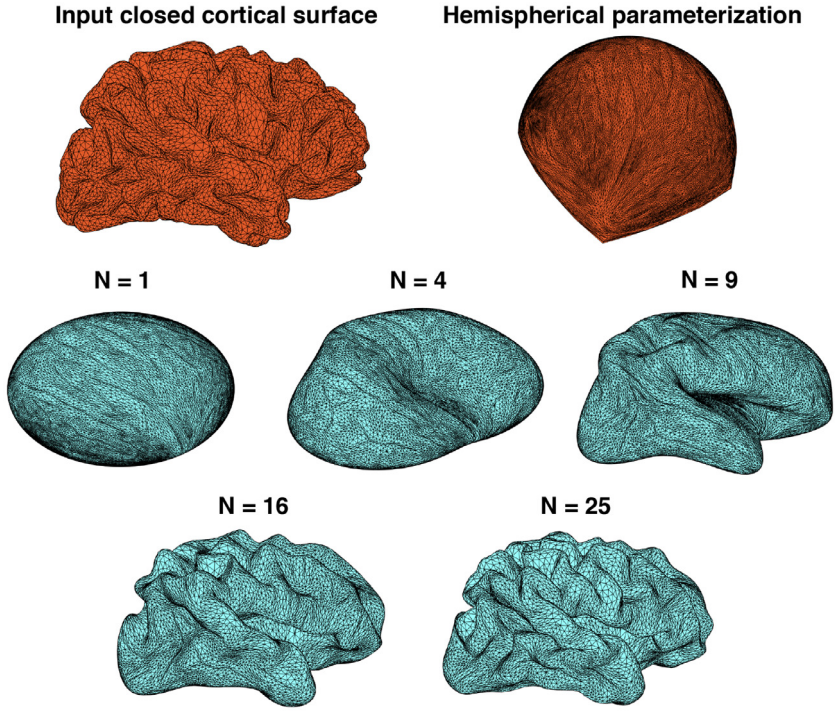

Fig. 14. A closed brain cortical surface (top left), the hemispherical area-preserving parameterization (top right), and the HSH reconstructions with maximum order $N = 1, 4, 9, 16, 25$ (bottom).

7. Conclusions

In this work, we have proposed a novel framework for the 3D shape description of open and closed hemisphere-like anatomical surfaces. The key idea of our approach is to compute a hemispherical area-preserving parameterization of any input surface onto the unit hemisphere, which allows us to utilize the HSH basis functions for the shape description and reconstruction. We have demonstrated the effectiveness of our proposed framework using 60 hemispherical anatomical surfaces (20 closed brain surfaces, 20 closed skull surfaces, and 20 open scalp surfaces) constructed from human head MRI scans. For all the three types of surfaces, our framework achieves a significant improvement in the surface reconstruction accuracy by 75%, 80% and 50% respectively when compared to the SH based approach. Therefore, our proposed framework may serve as a useful tool for the biomedical analysis of hemisphere-like anatomical objects.

Declaration of Competing Interest

None of the authors declares any conflict of interest.

CRediT authorship contribution statement

Amita Giri: Conceptualization, Methodology, Validation, Formal analysis, Writing - original draft. **Gary P.T. Choi:** Conceptualization, Methodology, Validation, Formal analysis, Writing - original draft. **Lalan Kumar:** Formal analysis, Writing - original draft.

Acknowledgements

This work was supported in part by the Prime Ministers Research Fellowship (PMRF), Government of India (to A. Giri), and the National Science Foundation under Grant No. DMS-2002103 (to G. P. T. Choi).

References

[1] L. Mak, S. Grandison, R.J. Morris, An extension of spherical harmonics to region-based rotationally invariant descriptors for molecular shape description and comparison, J. Mol. Graph. Model. 26 (7) (2008) 1035–1045.
[2] M. Nitzken, M. Casanova, G. Gimel'farb, F. Khalifa, A. Elnakib, A.E. Switala, A. El-Baz, 3D shape analysis of the brain cortex with application to autism, in: Proceedings of the 8th IEEE International Symposium on Biomedical Imaging: From Nano to Macro, 2011, pp. 1847–1850.
[3] M. Nitzken, M. Casanova, G. Gimel'farb, A. Elnakib, F. Khalifa, A. Switala, A. El-Baz, 3D shape analysis of the brain cortex with application to dyslexia, in: 2011 18th IEEE International Conference on Image Processing, 2011, pp. 2657–2660.
[4] B.N. Cuffin, EEG localization accuracy improvements using realistically shaped head models, IEEE Trans. Biomed. Eng. 43 (3) (1996) 299–303.
[5] A. Giri, L. Kumar, T. Gandhi, Head harmonics based EEG dipole source localization, in: 2019 53rd Asilomar Conference on Signals, Systems, and Computers, 2019, pp. 2149–2153.
[6] C. Purcell, T. Mashiko, K. Odaka, K. Ueno, Describing head shape with surface harmonic expansions, IEEE Trans. Biomed. Eng. 38 (3) (1991) 303–306.
[7] M. Kazhdan, T. Funkhouser, S. Rusinkiewicz, Rotation invariant spherical harmonic representation of 3D shape descriptors, in: Symposium on Geometry Processing, 6, 2003, pp. 156–164.
[8] M. Jallouli, W.B. Khalifa, A.B. Mabrouk, M.A. Mahjoub, Toward new spherical harmonic Shannon entropy for surface modeling, in: International Conference on Computer Analysis of Images and Patterns, Springer, 2019, pp. 38–48.
[9] L. Shen, M.K. Chung, Large-scale modeling of parametric surfaces using spherical harmonics, in: Third International Symposium on 3D Data Processing, Visualization, and Transmission (3DPVT'06), IEEE, 2006, pp. 294–301.
[10] L. Shen, H. Farid, M.A. McPeek, Modeling three-dimensional morphological structures using spherical harmonics, Evolution 63 (4) (2009) 1003–1016.
[11] G. Gerig, M. Styner, D. Jones, D. Weinberger, J. Lieberman, Shape analysis of brain ventricles using SPHARM, in: Proceedings of the IEEE Workshop on Mathematical Methods in Biomedical Image Analysis (MMBIA 2001), IEEE, 2001, pp. 171–178.
[12] M. Styner, I. Oguz, S. Xu, C. Brechbühler, D. Pantazis, J.J. Levitt, M.E. Shenton, G. Gerig, Framework for the statistical shape analysis of brain structures using SPHARM-PDM, Insight J (1071) (2006) 242.
[13] K. Zhou, H. Bao, J. Shi, 3D surface filtering using spherical harmonics, Comput. Aided Des. 36 (4) (2004) 363–375.
[14] M. Jallouli, M. Zemni, A.B. Mabrouk, M.A. Mahjoub, Toward recursive spherical harmonics-issued bi-filters: Part I: theoretical framework, Soft Comput. 23 (20) (2019) 10415–10428.
[15] M. Jallouli, W.B.H. Khélifa, A.B. Mabrouk, M.A. Mahjoub, Toward recursive spherical harmonics issued bi-filters: Part II: an associated spherical harmonics entropy for optimal modeling, Soft Comput. 24 (7) (2020) 5231–5243.
[16] M. Jallouli, W.B. Khalifa, A.B. Mabrouk, M.A. Mahjoub, Assessment of global left ventricle deformation using recursive spherical harmonics, in: The International Conference on Natural Computation, Fuzzy Systems and Knowledge Discovery, Springer, 2019, pp. 498–505.
[17] S.H. Westin, J.R. Arvo, K.E. Torrance, Predicting reflectance functions from complex surfaces, Comput. Graph. (ACM) 26 (2) (1992) 255–264.
[18] T.-T. Wong, P.-A. Heng, S.-H. Or, W.-Y. Ng, Image-based rendering with controllable Illumination, in: Rendering Techniques, Springer, 1997, pp. 13–22.
[19] J. Kautz, J. Snyder, P.-P.J. Sloan, Fast arbitrary BRDF shading for low-frequency lighting using spherical harmonics, Rendering Techniques 2 (2002) 291–296.
[20] R. Basri, D.W. Jacobs, Lambertian reflectance and linear subspaces, IEEE Trans. Pattern Anal. Mach. Intell. 25 (2) (2003) 218–233.
[21] R. Basri, D. Jacobs, I. Kemelmacher, Photometric stereo with general, unknown lighting, Int. J. Comput. Vis. 72 (3) (2007) 239–257.
[22] L. Zhang, D. Samaras, Pose invariant face recognition under arbitrary unknown lighting using spherical harmonics, in: International Workshop on Biometric Authentication, 2004, pp. 10–23.
[23] R. Ramamoorthi, P. Hanrahan, An efficient representation for irradiance environment maps, in: Proceedings of the 28th Annual Conference on Computer Graphics and Interactive Techniques, 2001, pp. 497–500.
[24] A. Giri, L. Kumar, T. Gandhi, EEG dipole source localization in hemispherical harmonics domain, in: 2018 Asia-Pacific Signal and Information Processing Association Annual Summit and Conference (APSIPA ASC), 2018, pp. 679–684.
[25] P. Gautron, J. Krivanek, S.N. Pattanaik, K. Bouatouch, A novel hemispherical basis for accurate and efficient rendering, in: Proceedings of the Fifteenth Eurographics Conference on Rendering Techniques, 2004, pp. 321–330.
[26] D.V. Vranic, D. Saupe, J. Richter, Tools for 3D-object retrieval: Karhunen-loeve transform and spherical harmonics, in: 2001 IEEE Fourth Workshop on Multimedia Signal Processing (Cat. No. 01TH8564), IEEE, 2001, pp. 293–298.
[27] L. Shen, F. Makedon, Spherical mapping for processing of 3D closed surfaces, Image Vision Comput. 24 (7) (2006) 743–761.
[28] H. Huang, L. Zhang, D. Samaras, L. Shen, R. Zhang, F. Makedon, J. Pearlman, Hemispherical harmonic surface description and applications to medical image analysis, in: Third International Symposium on 3D Data Processing, Visualization, and Transmission (3DPVT'06), 2006, pp. 381–388.
[29] S.Y. Elhabian, H. Rara, A.A. Farag, Towards accurate and efficient representation of image irradiance of convex-lambertian objects under unknown near lighting, in: Proceedings of the 2011 IEEE International Conference on Computer Vision, 2011, pp. 1732–1737.
[30] M. Manfredi, G. Bearman, G. Williamson, D. Kronkright, E. Doehne, M. Jacobs, E. Marengo, A new quantitative method for the non-invasive documentation of morphological damage in paintings using RTI surface normals, Sensors 14 (7) (2014) 12271–12284.
[31] C. Brechbühler, G. Gerig, O. Kübler, Parametrization of closed surfaces for 3-D shape description, Comput. Vis. Image Underst. 61 (2) (1995) 154–170.
[32] M.S. Floater, K. Hormann, Surface parameterization: a tutorial and survey, Advances in Multiresolution for Geometric Modelling (2005) 157–186.
[33] A. Sheffer, E. Praun, K. Rose, et al., Mesh parameterization methods and their applications, Found. Trends Comput. Graph. Vis. 2 (2) (2007) 105–171.
[34] M. Desbrun, M. Meyer, P. Alliez, Intrinsic parameterizations of surface meshes, Comput. Graph. Forum 21 (3) (2002) 209–218.
[35] B. Lévy, S. Petitjean, N. Ray, J. Maillot, Least squares conformal maps for automatic texture atlas generation, ACM Trans. Graph. 21 (3) (2002) 362–371.
[36] G.P.T. Choi, Y. Chen, L.M. Lui, B. Chiu, Conformal mapping of carotid vessel wall and plaque thickness measured from 3D ultrasound images, Med. Biol. Eng. Comput. 55 (12) (2017) 2183–2195.
[37] G.P.T. Choi, Y. Leung-Liu, X. Gu, L.M. Lui, Parallelizable global conformal parameterization of simply-connected surfaces via partial welding, SIAM J. Imaging Sci. 13 (3) (2020) 1049–1083.
[38] S. Angenent, S. Haker, A. Tannenbaum, R. Kikinis, Conformal geometry and brain flattening, Med. Image Comput. Comput. Assist. Interv. (1999) 271–278.
[39] S. Haker, S. Angenent, A. Tannenbaum, R. Kikinis, G. Sapiro, M. Halle, Conformal surface parameterization for texture mapping, IEEE Trans. Vis. Comput. Graph. 6 (2) (2000) 181–189.
[40] X. Gu, Y. Wang, T.F. Chan, P.M. Thompson, S.-T. Yau, Genus zero surface conformal mapping and its application to brain surface mapping, IEEE Trans. Med. Imaging 23 (8) (2004) 949–958.
[41] R. Lai, Z. Wen, W. Yin, X. Gu, L.M. Lui, Folding-free global conformal mapping for genus-0 surfaces by harmonic energy minimization, J. Sci. Comput. 58 (3) (2014) 705–725.
[42] P.T. Choi, K.C. Lam, L.M. Lui, FLASH: Fast landmark aligned spherical harmonic parameterization for genus-0 closed brain surfaces, SIAM J. Imaging Sci. 8 (1) (2015) 67–94.
[43] G.P.-T. Choi, K.T. Ho, L.M. Lui, Spherical conformal parameterization of genus-0 point clouds for meshing, SIAM J. Imaging Sci. 9 (4) (2016) 1582–1618.
[44] X. Gu, S.-T. Yau, Computing conformal structures of surfaces, Commun. Inf. Syst. 2 (2) (2002) 121–146.

[45] M. Jin, J. Kim, F. Luo, X. Gu, Discrete surface RICCI flow, IEEE Trans. Vis. Comput. Graph. 14 (5) (2008) 1030–1043.
[46] P.T. Choi, L.M. Lui, Fast disk conformal parameterization of simply-connected open surfaces, J. Sci. Comput. 65 (3) (2015) 1065–1090.
[47] M.-H. Yueh, W.-W. Lin, C.-T. Wu, S.-T. Yau, An efficient energy minimization for conformal parameterizations, J. Sci. Comput. 73 (1) (2017) 203–227.
[48] G.P.-T. Choi, L.M. Lui, A linear formulation for disk conformal parameterization of simply-connected open surfaces, Adv. Comput. Math. 44 (1) (2018) 87–114.
[49] G. Zou, J. Hu, X. Gu, J. Hua, Authalic parameterization of general surfaces using Lie advection, IEEE Trans. Vis. Comput. Graph. 17 (12) (2011) 2005–2014.
[50] X. Zhao, Z. Su, X.D. Gu, A. Kaufman, J. Sun, J. Gao, F. Luo, Area-preservation mapping using optimal mass transport, IEEE Trans. Vis. Comput. Graph. 19 (12) (2013) 2838–2847.
[51] S. Nadeem, Z. Su, W. Zeng, A. Kaufman, X. Gu, Spherical parameterization balancing angle and area distortions, IEEE Trans. Vis. Comput. Graph. 23 (6) (2017) 1663–1676.
[52] A. Pumarola, J. Sanchez-Riera, G. Choi, A. Sanfeliu, F. Moreno-Noguer, 3DPeople: modeling the geometry of dressed humans, Proc. IEEE Int. Conf. Comput. Vis. (2019) 2242–2251.
[53] L. Cui, X. Qi, C. Wen, N. Lei, X. Li, M. Zhang, X. Gu, Spherical optimal transportation, Comput. Aided Des. 115 (2019) 181–193.
[54] G.P.T. Choi, C.H. Rycroft, Density-equalizing maps for simply connected open surfaces, SIAM J. Imaging Sci. 11 (2) (2018) 1134–1178.
[55] G.P.T. Choi, B. Chiu, C.H. Rycroft, Area-preserving mapping of 3D carotid ultrasound images using density-equalizing reference map, IEEE Trans. Biomed. Eng. 67 (9) (2020) 1507–1517.
[56] M.-H. Yueh, W.-W. Lin, C.-T. Wu, S.-T. Yau, A novel stretch energy minimization algorithm for equiareal parameterizations, J. Sci. Comput. 78 (3) (2019) 1353–1386.
[57] D.S. Marcus, A.F. Fotenos, J.G. Csernansky, J.C. Morris, R.L. Buckner, Open access series of imaging studies: longitudinal MRI data in nondemented and demented older adults, J. Cogn. Neurosci. 22 (12) (2010) 2677–2684.
[58] R. Oostenveld, P. Fries, E. Maris, J.-M. Schoffelen, Fieldtrip: open source software for advanced analysis of MEG, EEG, and invasive electrophysiological data, Comput. Intell. Neurosci. 2011 (2011) 156869.
[59] W.E. Byerly, Spherical Harmonics, in An Elementary Treatise on Fourier's Series, and Spherical, Cylindrical, and Ellipsoidal Harmonics, with Applications to Problems in Mathematical Physics. (1959) 195–218.
[60] G. Szeg, Orthogonal Polynomials, 23, American Mathematical Society, 1939.
[61] T.D. Abhayapala, D.B. Ward, Theory and design of high order sound field microphones using spherical microphone array, in: 2002 IEEE International Conference on Acoustics, Speech, and Signal Processing, 2, 2002, pp. 1949–1952.
[62] Z. Ben-Hur, D.L. Alon, B. Rafaely, R. Mehra, Loudness stability of binaural sound with spherical harmonic representation of sparse head-related transfer functions, EURASIP J. Audio Speech Music Process. 2019 (1) (2019) 5.
[63] E. Niedermeyer, F.L. da Silva, Electroencephalography: Basic principles, clinical applications, and related fields, Lippincott Williams & Wilkins, 2005.
[64] I. Oguz, J. Cates, M. Datar, B. Paniagua, T. Fletcher, C. Vachet, M. Styner, R. Whitaker, Entropy-based particle correspondence for shape populations, Int. J. Comput. Assist. Radiol. Surg. 11 (7) (2016) 1221–1232.
[65] S. Durrleman, M. Prastawa, N. Charon, J.R. Korenberg, S. Joshi, G. Gerig, A. Trouvé, Morphometry of anatomical shape complexes with dense deformations and sparse parameters, Neuroimage 101 (2014) 35–49.
[66] J. Cates, S. Elhabian, R. Whitaker, ShapeWorks: particle-based shape correspondence and visualization software, in: Statistical Shape and Deformation Analysis, Elsevier, 2017, pp. 257–298.